ACS OMEGA

http://pubs.acs.org/journal/acsodf

Article

# Porous Carbon Nanofibers with Heteroatoms Doped by Electrospinning Exhibit Excellent Acetone and Carbon Dioxide Adsorption Performance: The Contributions of Pore Structure and Functional Groups

Rui Shi, Baogen Liu, Yuwei Jiang, Xiang Xu, Huijun Wang, Zheng Zeng,* and Liqing Li*

Cite This: *ACS Omega* 2021, 6, 30716−30725

Read Online

ACCESS | Metrics & More | Article Recommendations | Supporting Information

**ABSTRACT:** Rich chemical properties and a well-developed pore structure are the key factors of porous materials for gas storage. Herein, rich heteroatom-doped porous carbon nanofibers ($U_1K_2$-X) with a large surface area were prepared by electrospinning followed by potassium hydroxide (KOH) activation. Low-cost urea was chosen as the nitrogen source and structural guiding agent. $U_1K_2$-X have a high specific surface area (628−2688 $m^2$ $g^{-1}$), excellent pore volume (0.468−1.571 $cm^3$ $g^{-1}$), and abundant nitrogen (2.5−12.8 atom %) and oxygen (4.5−12.5 atom %) contents. Acetone and carbon dioxide were used as target adsorbents to evaluate the adsorption properties of $U_1K_2$-X by experiments. These $U_1K_2$-X exhibit excellent adsorption performance (260.03−955.74 mg $g^{-1}$, 25 °C, 18 kPa) and multilayer adsorption (the adsorption layer number $n$ > 2) for acetone, which is mainly attributed to the large specific surface area and pore volume. Besides this, the carbon dioxide uptake reached 2.73−3.34 mmol $g^{-1}$ at 25 °C. This was attributed to the combination of high nitrogen−oxygen contents and microporous structure. Furthermore, $U_1K_2$-X show the desirable repeatability. This study provides a new direction for the preparation of heteroatom-doped porous carbon nanofibers, which will be a promising material for gas adsorption.

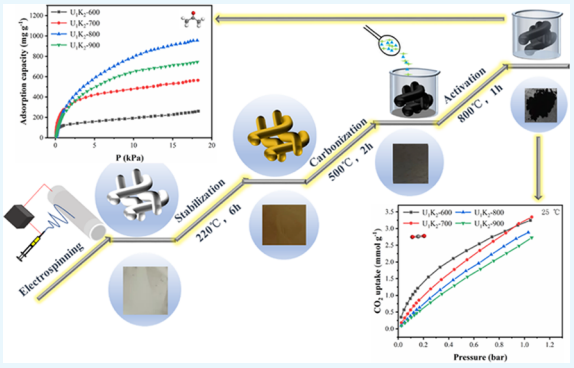


## 1. INTRODUCTION

Volatile organic compounds (VOCs) and greenhouse gas ($CO_2$) lead to harmful effects on the environment and human beings. It is worth mentioning that adsorption by porous carbon materials has been proved as one of the most effective methods for VOCs and $CO_2$ treatment.[1−3] Among the porous carbon materials, activated carbon fibers have attracted the attention of researchers because of their fibrous morphology, excellent pore structure, high adsorption capacity, and fast kinetics.[4,5]

A suitable pore structure and surface functional groups of adsorbents can promote the adsorption performance of VOCs and $CO_2$.[6,7] For instance, researchers[8−10] have reported that narrow micropore size (0.8 nm) is the key factor for $CO_2$ adsorption. Xu[11] investigated the VOC adsorption among carbon sheets with different pore sizes (0.8−5.0 nm) by GCMC. The more effective pores for acetone adsorption at 18 kPa are in the range of 1.6−3.2 nm. However, activated carbon fibers are microporous materials with few mesopores or macropores.[12] The earlier-reported VOC adsorption capacities of electrospun-activated carbon fibers are relatively low.[13,14] It is thus significant to study how to develop hierarchical pores on activated carbon fibers for the adsorption of VOCs and $CO_2$. In addition, specific surface area and pore volume are the key factors for VOC adsorption.[15] While electrospun-activated carbon fibers are easier to obtain a large specific surface area, their fiber diameter is much smaller than that of the traditional commercial fiber.[16−18] The fibers are fabricated using polyacrylonitrile,[19] pitch,[20] and poly(vinyl alcohol)[21] as precursors commonly, followed by electrospinning, stabilization, carbonization, and activation.

Heteroatoms can enhance the interaction between VOCs, $CO_2$ molecules, and the adsorbent. Wang et al.[22] studied the $CO_2$ adsorption performance of nitrogen-containing porous carbon fibers (1.23−2.73% N) derived from polyimide fiber. The synergistic effects of nitrogen surface functional groups and narrow micropores play an important role in $CO_2$ adsorption. Gao et al.[23] found that nitrogen surface functional groups enhance the adsorption interaction between the carbon surface and the acetone molecule. All these studies ignored the role of

**Received:** August 24, 2021
**Accepted:** October 22, 2021
**Published:** November 4, 2021

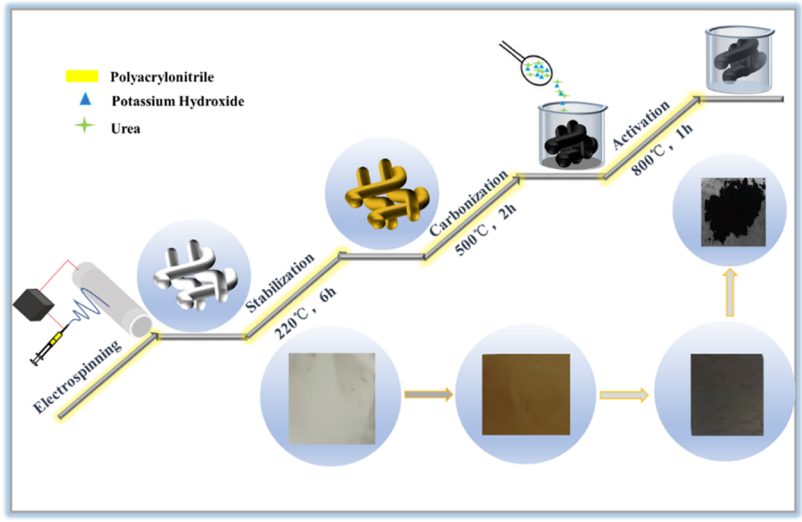


**Figure 1.** Formation process of $U_1K_2$-X.

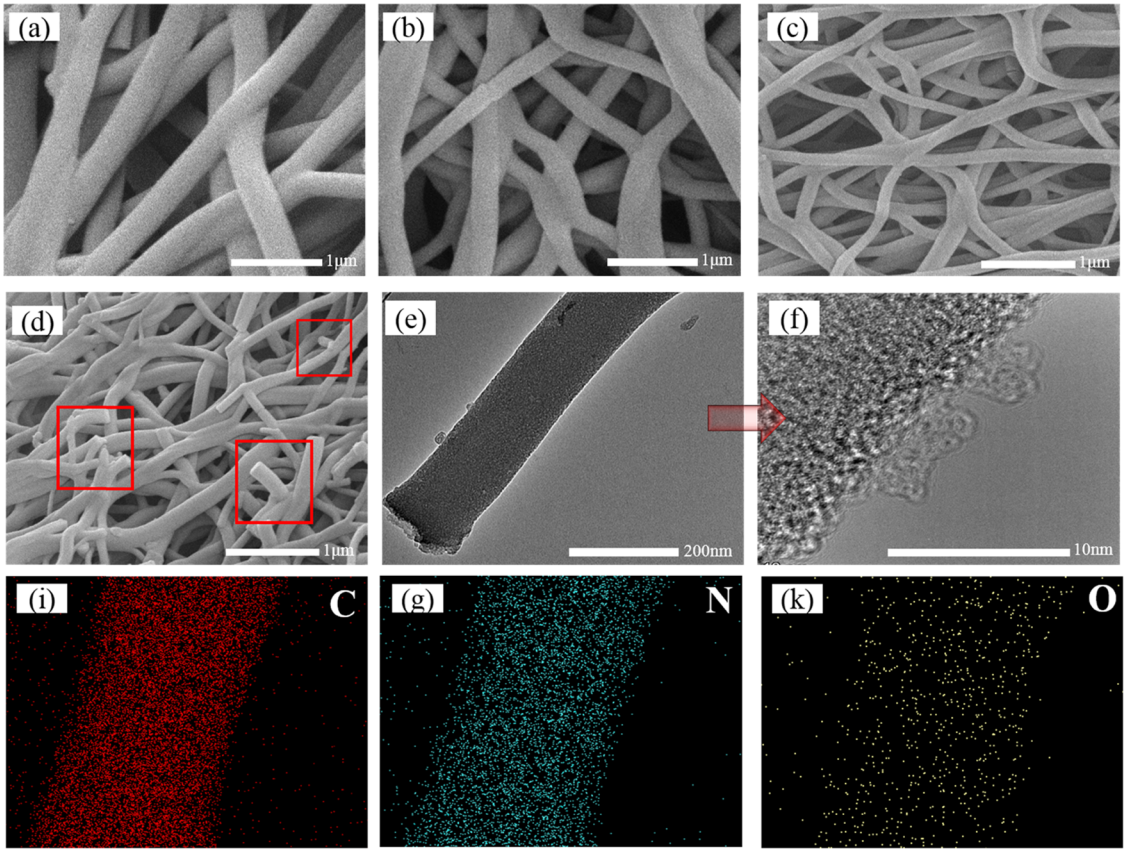


**Figure 2.** SEM (a–d) images: (a) $U_1K_2$-600, (b) $U_1K_2$-700, (c) $U_1K_2$-800, (d) $U_1K_2$-900, TEM images (e, f), and elemental mapping (i, k).

oxygen functional groups. However, oxygen functional groups have been considered as a factor that can improve the adsorption capacity of hydrophilic VOCs.[24] Meng et al.[25] prepared oxygen-containing activated carbon fibers using lignin; acetone showed a larger adsorption capacity (105.48 mg $g^{-1}$) in the competitive adsorption of toluene, acetone, and methanol.

Based on the above analysis, we have proposed a strategy to develop a series of porous carbon nanofibers through nitrogen–oxygen doping by electrospinning using potassium hydroxide (KOH) and urea as the activator and nitrogen source, respectively. The changes of the pore structures, which were observed after the activation process at 600–900 °C, were described by X-ray diffraction and Raman spectroscopy, to reveal the KOH activation mechanism. Acetone and $CO_2$ were selected as the target adsorbates, and their adsorption performances on the obtained samples were comprehensively investigated. Moreover, we also combined the physicochemical properties with the adsorption capacities of acetone and $CO_2$ to further understand their adsorption mechanism.



https://doi.org/10.1021/acsomega.1c04618
ACS Omega 2021, 6, 30716–30725

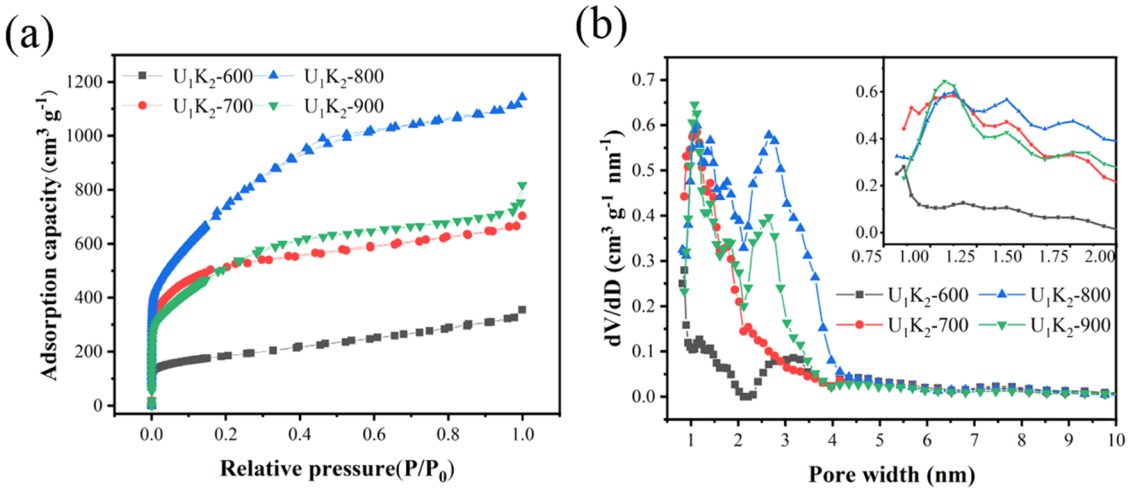


**Figure 3.** (a) $N_2$ adsorption−desorption isotherms and (b) pore-size distribution of $U_1K_2$-X.

## 2. RESULTS AND DISCUSSION

**2.1. Synthesis of $U_1K_2$-X.** As shown in Figure 1, The carbonized mats (ACFs) undergo the processes of electrospinning, stabilization, and carbonization to form the precursor of porous carbon fibers. Thermogravimetric analysis (TGA) is used to better reveal the high-temperature conversion reaction of the ACFs, urea, and their mixture (ACFs + urea) as shown in Figure S1. In the temperature range of 180−210 °C, the weights of urea and ACFs + urea show the same trend of drastic reduction, which is mainly due to the decomposition of urea at 150 °C, and the following reactions occur during the urea decomposition: $CO(NH_2)_2 \rightarrow NH_3 + HNCO$ and $HNCO \rightarrow H_2O + CO_2 + NH_3$.[26] The weight of ACFs (39.2%) decrease more intensely than that of ACFs + urea (19.3%) between 500 and 1000 °C. In this temperature range, urea decomposes and forms graphitic carbon nitride nanosheets at 500 °C, and ACFs can infiltrate and be carbonized. Above 700 °C, the infiltrated ACFs transform into graphene structure, and graphitic carbon nitride decomposes into $NH_3$ and $C_2N_2$, which are doped by nitrogen into $U_1K_2$-X.[27] Hence, urea plays the roles of nitrogen source and a structure-directing agent.

KOH usually reacts with carbon materials during the activation.[28−30] The KOH and C redox reaction occurs and the carbon framework is etched; potassium ions are inserted above 700 °C.[27,31] Finally, 5% hydrochloric acid is used to wash away the impurities on the surface of $U_1K_2$-X.

**2.2. Characterization of $U_1K_2$-X.** The surface morphology of $U_1K_2$-X is characterized by scanning electron microscopy (SEM) and transmission electron microscopy (TEM) as shown in Figure 2. The average diameter of $U_1K_2$-X decreases with the increase of the activation temperature,[32] and the average diameter changes from 220 to 169 nm, which is calculated by randomly selecting 50 fibers from SEM images (Figure 2a−d). Some shorter carbon nanofibers are found in $U_1K_2$-900, suggesting that the heat treatment led to an increased number of shorter carbon nanofibers.[33] The pore structures are further studied by TEM. As revealed in Figure 2e,f, a large number of pores are present on the carbon nanofiber. Elemental mapping of $U_1K_2$-800 (Figure 2i−k) shows a uniform distribution of C, N, and O, proving that heteroatom-doped porous carbon nanofibers have been synthesized successfully.

The $N_2$ adsorption−desorption isotherms of $U_1K_2$-X are shown in Figure 3a. All $U_1K_2$-X display type I combined with type IV isotherms, suggesting an obvious micro−mesopore structure.[11] The pore-size distributions (PSDs) are determined via the non-local density functional theory (NLDFT) method. The PSDs of $U_1K_2$-600 (0.8 and 2.6 nm) exhibit two peaks. Meanwhile, $U_1K_2$-700 exhibits five peaks (0.8, 1.1, 1.4, 1.7, and 2.2 nm), and $U_1K_2$-800 and $U_1K_2$-900 exhibit four peaks nearly at 1.1, 1.4, 1.7, and 2.6 nm (Figure 3b). The specific surface area is calculated by Brunauer−Emmett−Teller (BET) method, ranging from 627 m$^2$ g$^{-1}$ (600 °C) to 2688 m$^2$ g$^{-1}$ (800 °C). The total pore volume (0.468−1.571 cm$^3$ g$^{-1}$) and micropore pore volume (0.011−0.389 cm$^3$ g$^{-1}$) increase steadily with the increase in carbonization temperature from 600 to 800 °C, then slightly decrease at 900 °C. Herein, the pore structure of carbon nanofibers can be regulated by adjusting the activation temperature. All textural parameters are shown in Table 1.

**Table 1. Textural Properties of the Samples**[a]

| sample | $S_{BET}$ (m$^2$ g$^{-1}$) | $V_{total}$ (cm$^3$ g$^{-1}$) | $V_{micro}$ (cm$^3$ g$^{-1}$) | $V_{micro}/V_{meso(\%)}$ |
|---|---|---|---|---|
| $U_1K_2$-600 | 628 | 0.468 | 0.011 | 2.40 |
| $U_1K_2$-700 | 1757 | 0.931 | 0.210 | 29.13 |
| $U_1K_2$-800 | 2688 | 1.571 | 0.389 | 32.91 |
| $U_1K_2$-900 | 1845 | 1.028 | 0.275 | 36.52 |

[a]Note: $S_{BET}$ values are calculated by BET analysis and *t*-plot analysis.

In order to further study the structural changes of $U_1K_2$-X at different activation temperatures, the X-ray diffraction (XRD) patterns are shown in Figure 4a. The peak located at 25° corresponds to (002), indicating that the pore walls consist of nanoscale graphene-like units,[34] and the peak (46°) corresponds to (100), suggesting the presence of planar graphite carbon.[35] These intensities of peaks decrease with the increase of the activation temperature, indicating the increase in the irregularity of layer structures.[32] The structural parameters obtained from the XRD patterns are shown in Table 2. The $d_{002}$ increases from 0.377 to 0.417 nm with the increase in activation temperature from 600 to 900 °C, which is larger than that of an ideal single graphene layer ($d_{002}$ = 0.335 nm), which may be the reason for the enlargement of the micropores (Table 1).[36] The increase of $d_{002}$ also shows that there are heteroatoms embedded in $U_1K_2$-X during the activation. With increase of the activation temperature, $L_c$ and $L_{a,X}$ decrease first and then increase slightly, while the stacking number decreases. A reduction in the stacking


https://doi.org/10.1021/acsomega.1c04618
ACS Omega 2021, 6, 30716−30725

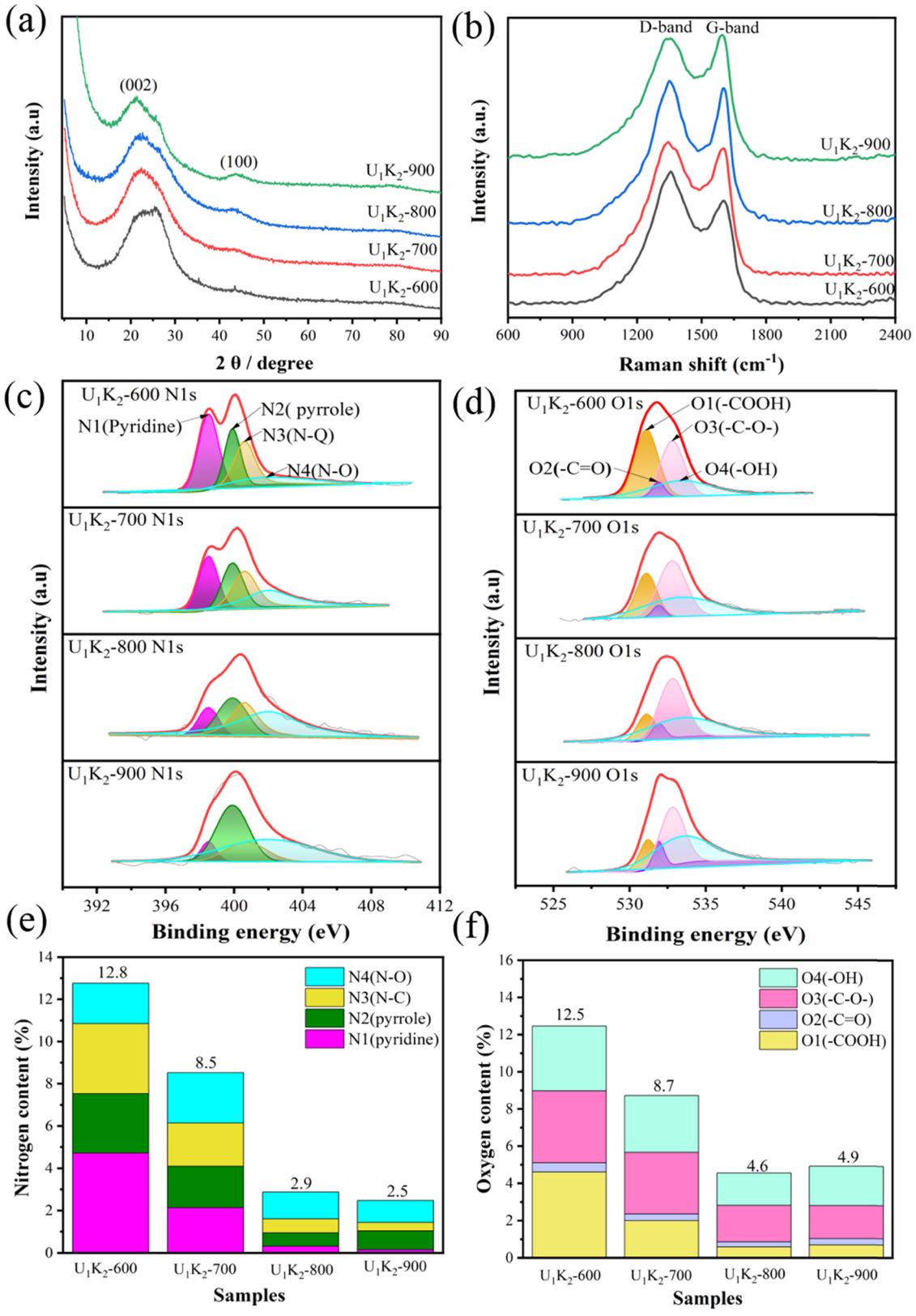


**Figure 4.** (a) X-ray diffraction pattern, (b) Raman spectra of $U_1K_2$-X, (c) fitted X-ray photoelectron spectroscopy (XPS) N 1s spectra, (d) fitted XPS O 1s spectra, (e) nitrogen composition, and (f) oxygen composition.

number of nanoscale graphene-like layers gives rise to a discontinuous PSD with a peak-to-peak difference of approximately 0.3 nm (Figure 3b). Consequently, nanoscale graphene-like layers are gasified one-by-one upon activation with KOH at different temperatures.[32]

All Raman spectra of $U_1K_2$-X show two characteristic peaks as shown in Figure 4b. The D-band (1360 $cm^{-1}$) and G-band



https://doi.org/10.1021/acsomega.1c04618
ACS Omega 2021, 6, 30716−30725

**Table 2. Structural Parameters of $U_1K_2$-X[a]**

| | XRD | | | Raman spectroscopy | |
|---|---|---|---|---|---|
| samples | $d_{002}$/nm | $L_c$/nm | stacking number | $L_{a,X}$/nm | $I_D/I_G$ |
| $U_1K_2$-600 | 0.377 | 0.61 | 1.61 | 1.26 | 1.28 |
| $U_1K_2$-700 | 0.391 | 0.49 | 1.25 | 1.02 | 1.05 |
| $U_1K_2$-800 | 0.392 | 0.47 | 1.20 | 0.99 | 1.05 |
| $U_1K_2$-900 | 0.417 | 0.48 | 1.15 | 0.97 | 0.97 |

[a]Note: (a) $d_{002}$ was calculated by Bragg's law. (b) $L_c$ and $L_{a,X}$ were calculated by Scherrer's equation. (c), the stacking number was determined by dividing $L_c$ by $d_{002}$.

(1591 $cm^{-1}$) originate from the defective graphene structure and highly crystalline graphene structure, respectively.[37,38] When the activation temperature increases from 600 to 900 °C, the ratio of $I_D/I_G$ decreases from 1.28 to 0.97, indicating that the graphitization degree of $U_1K_2$-X increases with the increase in temperature from 600 to 900 °C.

The XPS spectra associated with nitrogen and oxygen atomic content are shown in Figure 4c,f. The XPS spectra of $U_1K_2$-X show obvious N 1s and O 1s peaks (Figure 4c,d), implying the presence of nitrogen and oxygen atoms. With the increase of activation temperature, the atomic ratios of N and O decrease

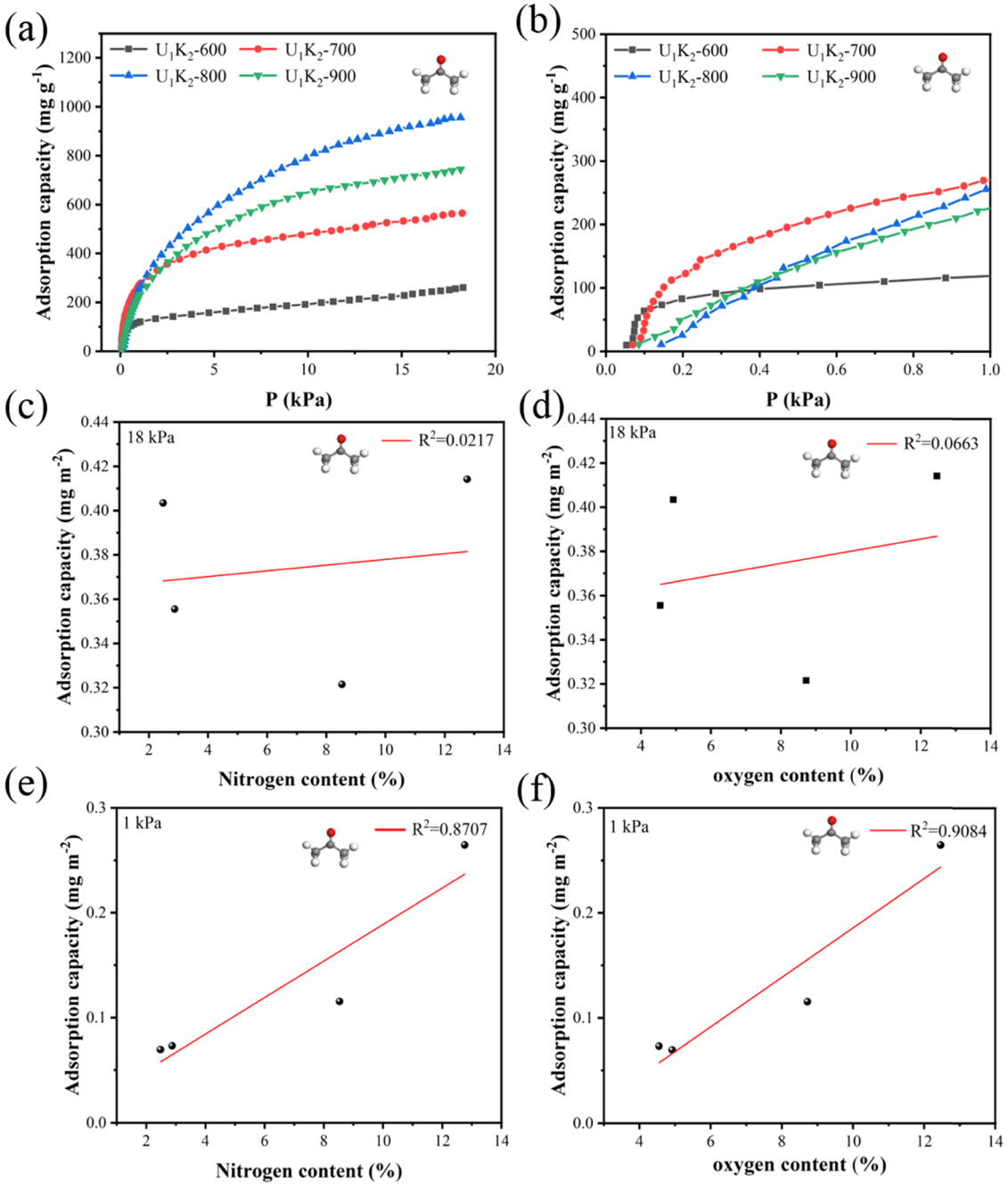


**Figure 5.** (a) Acetone isothermal adsorption at 25 °C and 18 kPa, (b) acetone isothermal adsorption at 25 °C and 1.0 kPa; relation between (c) nitrogen content and adsorption capacity per unit specific surface area at 18 kPa, (d) oxygen content and per unit specific surface area adsorption capacity at 18 kPa, (e) nitrogen content and per unit specific surface area adsorption capacity at 1 kPa, and (f) oxygen content and per unit specific surface area adsorption capacity at 1 kPa for acetone.



https://doi.org/10.1021/acsomega.1c04618
ACS Omega 2021, 6, 30716−30725

from 12.8 to 2.5 atom % and 12.5 to 4.6 atom %, respectively (Figure 4e,f). The nitrogen functional groups are mainly pyridine, pyrrole, graphite nitrogen (N−C), and oxidized nitrogen (N−O), of which pyridine and pyrrole can be used as adsorption sites for improving the gas adsorption.[39,40] The oxygen functional groups mainly consist of hydroxyl (−OH), carbonyl (−C═O), carbon and oxygen single bond (−C−O−), and carboxyl (−COOH), which can significantly enhance the interaction intensity between VOCs and the carbon surface.[24]

**2.3. Adsorption Characteristics.** *2.3.1. Acetone Adsorption.* The acetone adsorption isotherms on $U_1K_2$-X are shown in Figure 5a,b. The acetone adsorption capacity at 25 °C and 18 kPa follows the order $U_1K_2$-800 (955.74 mg $g^{-1}$) > $U_1K_2$-900 > $U_1K_2$-700 > $U_1K_2$-600 (260.03 mg $g^{-1}$). Compared with the previously reported adsorbents (Table 3), $U_1K_2$-X show a better acetone adsorption performance. However, the acetone adsorption capacity at 25 °C and 1 kPa is in a different order. Despite the lowest surface area and total pore volume, $U_1K_2$-600, having the highest nitrogen−oxygen content, displays the highest acetone adsorption capacity at a relatively low pressure.

**Table 3. Comparison of Adsorption Capacity for Acetone**

| adsorbents | $Q_e$ (mg $g^{-1}$) | $T$ (°C) | pressure (kPa) | references |
|---|---|---|---|---|
| $U_1K_2$-800 | 955.74 | 25 | 18 | this work |
| $U_1K_2$-900 | 744.28 | 25 | 18 | this work |
| $U_1K_2$-700 | 564.84 | 25 | 18 | this work |
| $U_1K_2$-600 | 260.03 | 25 | 18 | this work |
| ZCN600 | 417.00 | 25 | 18 | 43 |
| PC-800 | 257.29 | 25 | 18 | 44 |
| NP-1-900 | 789.00 | 25 | 18 | 23 |
| PC | 281.68 | 25 | 18 | 24 |

Linear fitting is carried out to reflect the coupling performance of the specific surface area, pore structures, and functional groups of $U_1K_2$-X on acetone adsorption. There is a good relationship ($R^2$ > 0.97, Figure S2a,b) between the adsorption capacity and total pore volume, and specific surface area, revealing that the total pore volume and specific surface area have a positive effect on the adsorption of acetone because a larger specific surface area can provide more adsorption sites for acetone molecules. To further analyze the adsorption behavior of acetone in different pores, the adsorption capacity of acetone at 18 and 1 kPa is correlated with the cumulative pore volume of different pore sizes, as shown in Figure S2c,d, respectively. The pore volume ($V_{2-5\ nm}$) of the narrow mesopore is the main factor for the adsorption capacity enhancement at 18 kPa ($R^2$ = 0.8226); this may be due to the formation of multilayer adsorption sites in the mesopore.[11] But the adsorption capacity of acetone has a good linear relationship with the volume of micropores at 1 kPa ($R^2$ = 0.9777), not the narrow mesopore ($R^2$ = 0.2654), resulting from the reduced interaction between the acetone molecule and the adjacent pore wall as the pore size increases.[41]

The adsorption capacities of acetone per unit specific surface area at 18 and 1 kPa are correlated with the nitrogen and oxygen content, respectively (Figure 5c,f). The adsorption capacity of acetone per unit specific surface area has no obvious linear relationship with the nitrogen and oxygen functional groups at 18 kPa, but they have a good linear relationship at 1 kPa ($R^2$ > 0.87). These results indicate that nitrogen and oxygen functional groups are more effective at low pressure, because the affinity between $U_1K_2$-X and acetone is improved. Specifically, all kinds of oxygen functional groups can promote the adsorption capacity ($R^2$ > 0.7346), due to the van der Waals force,[24] while nitrogen functional groups enhance the interaction between the carbon surface and acetone molecule by hydrogen bonding;[15] N4 has no significant promoting effect.

The experimental data are fitted with the L−F model and *n*-layer BET model in order to better analyze the adsorption behavior of $U_1K_2$-X on acetone. The fitting results of the two models are shown in Figure S3 and Table S1. The experimental data are well fitted by the above two models, especially the *n*-layer BET model (maximum $R^2$ of 0.9991). The $n_1$ (L−F model) of $U_1K_2$-X is greater than 1, representing a heterogeneous surface and positive adsorption cooperativity.[42] The adsorption layer is limited by $n$ (*n*-layer BET model), and the value of $n$ increases from 2.0 to 3.3, indicating that the adsorption of acetone on $U_1K_2$-X is not limited by monolayer adsorption, which is mainly due to the existence of a large number of mesoporous pores.[23]

*2.3.2. Carbon Dioxide Adsorption.* The adsorption isotherms of $CO_2$ in $U_1K_2$-X are measured at 0 and 25 °C, and $CO_2$ uptake values are 4.61−5.45 and 2.72−3.34 mmol $g^{-1}$, respectively (Figure 6a,b). The $CO_2$ uptake of $U_1K_2$-700 is better than that of previously reported carbon materials (Table 4). For physical adsorption, a large specific surface area and pore volume are beneficial to adsorption. However, $U_1K_2$-800 with the highest specific surface area (2688 $m^2$ $g^{-1}$) and pore volume (1.571 $cm^3$ $g^{-1}$) shows a lower $CO_2$ uptake, while $U_1K_2$-600 with the highest nitrogen−oxygen content (12.8 and 12.5 atom %), the smallest specific surface area (627 $m^2$ $g^{-1}$), and pore volume (0.468 $cm^3$ $g^{-1}$) displays a larger $CO_2$ uptake. Therefore, the $CO_2$ uptake of $U_1K_2$-X is not mainly dependent on its pore structure. Figure S4 shows the relationship between the physicochemical properties and $CO_2$ uptake of $U_1K_2$-X. The adsorption capacity of $CO_2$ has no obvious linear relationship with the specific surface area ($R^2$ = 0.2957) and total pore volume ($R^2$ = 0.3306). However, compared with the total pore volume, the relationship between $V_{<0.9\ nm}$ ($V_{<0.9\ nm}$ represents the pore volume for a pore diameter less than 0.9 nm) and $CO_2$ uptake is more obvious ($R^2$ = 0.5721). Note that a narrow micropore (0.8 nm) yields the best correlation with $CO_2$ uptake.[45] In addition, it is worth noting that there is an interesting correlation between the $CO_2$ uptake and the nitrogen and oxygen contents ($R^2$ = 0.7090), indicating that the introduction of nitrogen and oxygen atoms on as-prepared carbon nanofibers is the key factor for the $CO_2$ adsorption performance. The roles of oxygen functional group and nitrogen functional group are reflected in Figure S4e,f, respectively. The nitrogen functional groups are positively correlated with the $CO_2$ uptake per unit specific surface area ($R^2$ > 0.8176), except for N4, while carboxyl (O1) and carbonyl (O2) groups can obviously promote the adsorption performance of $CO_2$ ($R^2$ > 0.9482), illustrating that the effect of oxygen functional groups on $CO_2$ adsorption can not be ignored.

The fitting results of the L−F model for $CO_2$ adsorption at 0 °C and 25 °C are shown in Figure 6a,b and Table S2. The experimental data are well fitted by the L−F model (maximum $R^2$ of 0.9999). $n_1$, which represents the sorption intensity, decreases with the decrease of nitrogen and oxygen contents (Figure 4e,f). The $n_1$ for $CO_2$ adsorption at 0 and 25 °C ranges from 1.14 to 1.98 and 1.06 to 1.54, respectively. It shows that $CO_2$ is adsorbed on $U_1K_2$-X well.[46] The adsorption cooperativity is positive, which is consistent with the relationship between nitrogen−oxygen contents and $CO_2$ uptake. The *ka* of


https://doi.org/10.1021/acsomega.1c04618
ACS Omega 2021, 6, 30716−30725

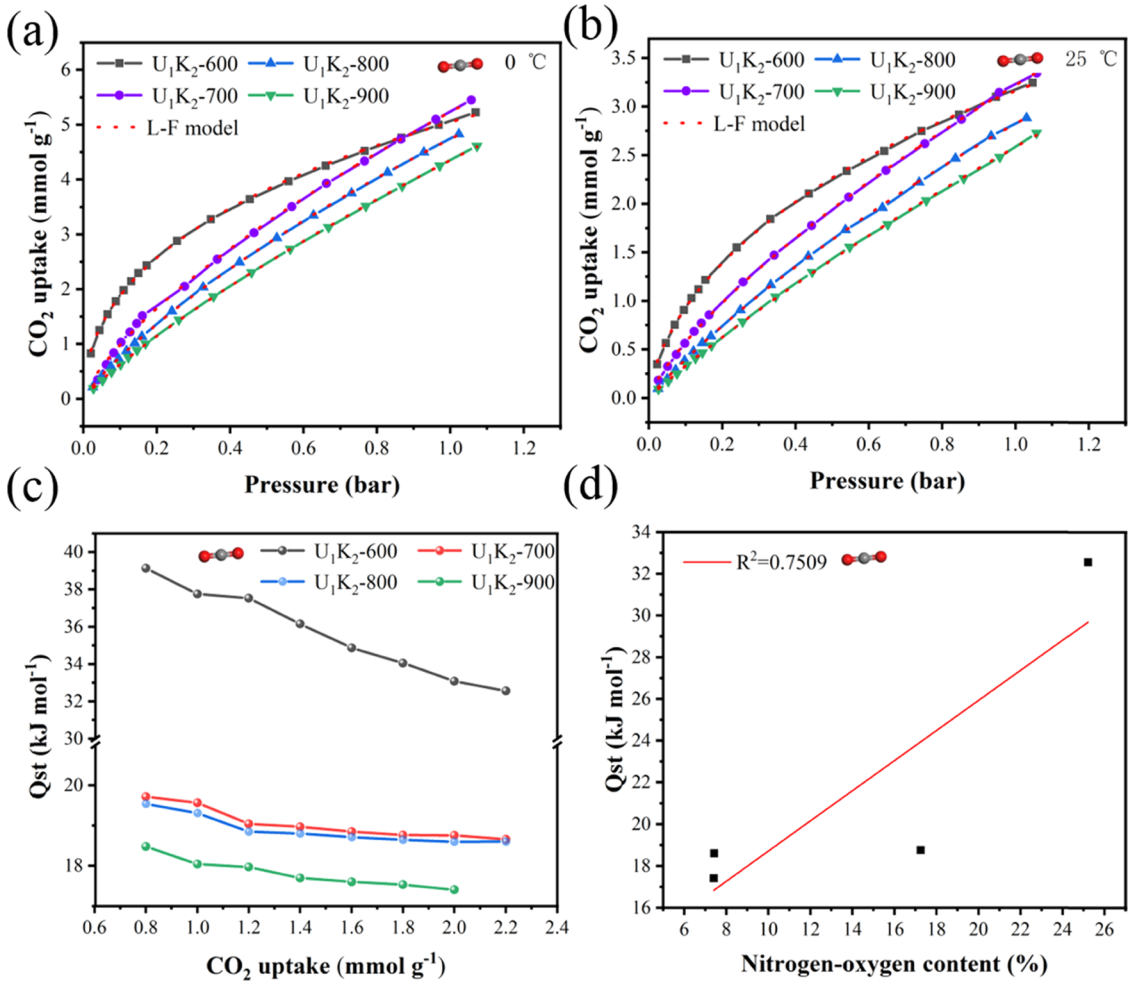


**Figure 6.** (a) $CO_2$ isothermal adsorption and fitting results of the L−F model at 0 °C and 1 bar, (b) $CO_2$ isothermal adsorption and fitting results of L−F at 25 °C and 1.0 bar, (c) isosteric heat of adsorption (*Qst*), and (d) relationship between *Qst* and nitrogen and oxygen contents.

**Table 4. Comparison of the Adsorption Capacities for $CO_2$**

| adsorbents | $Q_e$ (mmol $g^{-1}$) | *T* (°C) | pressure (kPa) | references |
|---|---|---|---|---|
| $U_1K_2$-700 | 3.34 | 25 | 100 | this work |
| ACNF/$Fe_2O_3$ | 1.50 | 25 | 100 | 50 |
| $ACNF_2$ | 2.68 | 25 | 100 | 51 |
| ACF-1 | 3.04 | 25 | 100 | 52 |
| T-GU-700-6 | 2.40 | 25 | 100 | 53 |

$U_1K_2$-600 is the largest, which is the Langmuir constant related to the affinity between the adsorbate molecule and solid sorbent,[47] showing that the interaction between $CO_2$ and $U_1K_2$-600 is the strongest.

To further reveal the adsorption behavior of $CO_2$ on $U_1K_2$-X, the isosteric heat of adsorption (*Qst*) is calculated by Clausius−Clapeyron equation.[48] As shown in Figure 6c, the *Qst* of $U_1K_2$-X gradually reduces with increasing surface coverages due to the

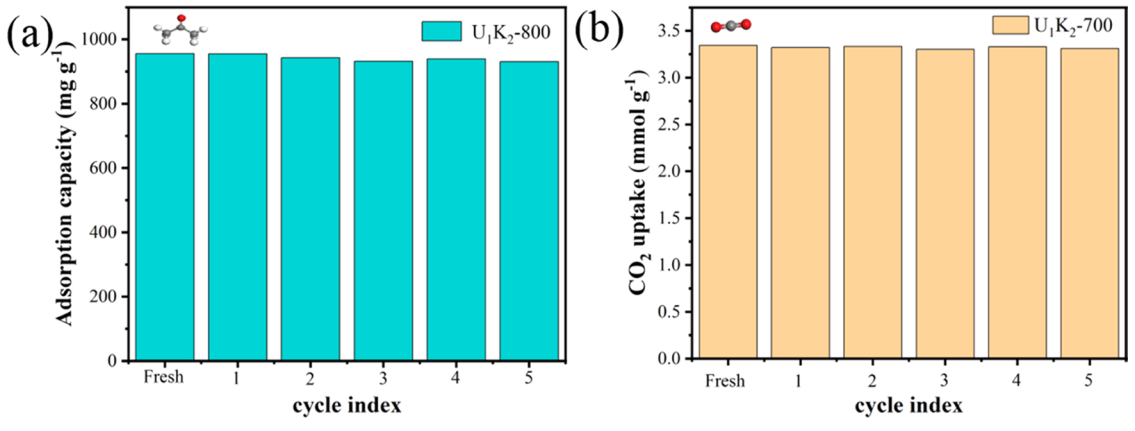


**Figure 7.** Cycle experimental results of (a) acetone on $U_1K_2$-800 and (b) $CO_2$ on $U_1K_2$-700.



https://doi.org/10.1021/acsomega.1c04618
ACS Omega 2021, 6, 30716−30725

reduced number of adsorption sites. The initial value of *Qst* is 18.47−39.13 kJ $mol^{-1}$, and $CO_2$ is easily adsorbed onto the adsorption point at low coverages. The initial *Qst* (39.13 kJ $mol^{-1}$) of $U_1K_2$-600 is between the isosteric heat of physisorption and chemisorption.[49] Therefore, the adsorption behavior of $U_1K_2$-600 is no longer a pure physical adsorption, which proves the key role of nitrogen−oxygen doping in $CO_2$ adsorption. Although the specific surface area of $U_1K_2$-700 is lower than that of $U_1K_2$-800, the *Qst* values of $U_1K_2$-700 and $U_1K_2$-800 are close to each other, which is also due to the stronger bonds occurring between the nitrogen−oxygen surface functional groups and $CO_2$ molecules. Furthermore, nitrogen and oxygen contents have a certain linear relationship with *Qst* (Figure 6d), which illustrates that high nitrogen and oxygen contents can enhance the sorbent−adsorbate interaction, thus increasing the value of *Qst*. In addition, the *Qst* values of $U_1K_2$-700, $U_1K_2$-800, and $U_1K_2$-900 are less than 20 kJ $mol^{-1}$, imply that the regeneration is relatively easy.

**2.4. Reusability of $U_1K_2$-X.** By comprehensively comparing the adsorption performances of $U_1K_2$-X for acetone and $CO_2$, $U_1K_2$-X containing rich nitrogen and oxygen functional groups were found to show an excellent adsorption performance of VOCs and $CO_2$. It is found that the sample with the highest adsorption capacity for acetone is $U_1K_2$-800, while that for $CO_2$ is $U_1K_2$-700. Under the same experimental conditions, $U_1K_2$-700 and $U_1K_2$-800 are tested for 5 cycles (the desorption conditions 150 °C, vacuum). The results are shown in Figure 7. After five adsorption−desorption cycles, there are some minor decreases in acetone adsorption capacity (<2.6%) and $CO_2$ uptake (<1.2%). Thus, $U_1K_2$-X have an excellent reusability.

## CONCLUSIONS

In summary, $U_1K_2$-X with a large specific surface area, pore volume, and nitrogen−oxygen content were prepared by electrospinning, stabilization, carbonation, and activation. Urea and potassium hydroxide act together at 600−900 °C to form a hierarchical pore structure. The physicochemical properties and adsorption performances for acetone and carbon dioxide were analyzed. $U_1K_2$-800 and $U_1K_2$-700 showed a superior adsorption capacity of acetone (955.74 mg $g^{-1}$, 25 °C) and $CO_2$ (3.34 mmol $g^{-1}$, 25 °C), respectively. The results revealed that the physical structure and surface chemistry of $U_1K_2$-X have a synergistic effect on the adsorption process. Consequently, the synthesized porous activated carbon nanofibers with nitrogen−oxygen doping would be a promising material in VOC and $CO_2$ adsorption.

## EXPERIMENT

**Materials.** Chemicals such as urea (99.9%), hydrochloric acid (37%), potassium hydroxide (KOH), and *N*,*N*-dimethylformamide (DMF, 99.5%, Mw 73.09) were supplied by Sinopharm Chemical Reagent Co. Ltd. Polyacrylonitrile (PAN, average Mw 150.000) was bought from McLean Co. Ltd. Nitrogen gas (99.995%) and $CO_2$ (99.99%) were purchased from Changsha High-Tech Gas Co. Ltd. Acetone was supplied by Sinopharm Chemical Reagent Co. Ltd.

**Preparation of Samples.** The activated carbon nanofibers can be obtained through electrospinning, stabilization, carbonization, and activation. PAN was dissolved in DMF and magnetically stirred at 50 °C for 6 h. The concentration of the polymer solution was 10%. Nine milliliters of PAN solution was placed in a syringe using a size 21 needle (inner diameter: 0.51 mm). Then it was electrospun into a nanofiber mat. The electrospinning conditions were as follows: voltage: 15 kV, syringe rate: 0.001 mm $s^{-1}$, collector rotation speed: 300 rpm, and collector distance: 10 cm. The fiber mat was stabilized at 220 °C for 6 h under air in a blast air oven, and the stabilized nanofiber mat was carbonized in a tube furnace at 500 °C at a heating rate of 5.0 °C $min^{-1}$ and held for 120 min under nitrogen atmosphere (flow rate 60 $m^3$ $h^{-1}$); these mats were named as ACFs.

1 g of ACFs, 1 g of urea, and 2 g of KOH were mixed and ground in a mortar, then heated in a tube furnace at 600, 700, 800, and 900 °C at a heating rate of 5.0 °C $min^{-1}$, and held for 60 min under nitrogen atmosphere (flow rate 60 $m^3$ $h^{-1}$). The black products were washed with hydrochloric acid solution (5%) and magnetically stirred for 36 h, then washed repeatedly with distilled water until neutral, and dried for 24 h in vacuum at 80 °C. The obtained activated carbon nanofibers were named as $U_1K_2$-X, where X is the activation temperature.

**Samples' Characterization.** Thermogravimetric analysis (TGA, SDT Q600, TA instruments, 10 °C $min^{-1}$) was used to investigate the thermal degradation process under nitrogen. The specific surface area and porosity measurements of the samples were determined from the $N_2$ adsorption/desorption isotherms using a static volumetric analyzer (JW-BK132Z, Beijing JWGB Sci & Tech Co., Ltd). Scanning electron microscopy (SEM, Helios NanoLab 600i, FEI Co.) and transmission electron microscopy (TEM, Titan G2 60-300) were used to characterize the morphologies, microstructures, and elemental mapping. X-ray photoelectron spectroscopy (XPS, Thermo Scientific K-$\alpha$) was used to analyze the composition and functional groups. The interlayer distance ($d_{002}$), stack height ($L_c$), and stack width ($L_{a,X}$) of a less-crystalline graphitic unit were evaluated by X-ray diffraction[32] (XRD, Cu/K$\alpha$ as the diffraction source, $\lambda$ = 0.15406 nm, Bruker D8 advance). The degree of graphitization was evaluated by Raman spectroscopy[54] (HORIBA Scientific LabRAM HR Evolution, $\lambda$ = 532 nm). The acetone adsorption isotherms at 25 °C and carbon dioxide adsorption isotherms at 25 and 0 °C were measured volumetrically by the JW-BK132Z static volumetric analyzer. The adsorption pressures of acetone and carbon dioxide range from 0 to 18 kPa and from 0 to 100 kPa, respectively.

**Adsorption Isotherm.** The Langmuir−Freundlich (L−F) model[55] can be used to evaluate the heterogeneity of the surface, and is defined as eq 1. The *n*-layer BET[56] model is commonly used to estimate multilayer adsorption in a gas−solid system, and is defined as eq 2.

$$q = \frac{Q_m k_a P^{1/n1}}{1 + k_a P^{1/n1}} \tag{1}$$

$$q = \frac{Q_m b\frac{P}{P_s}}{1 - \frac{P}{P_s}} \cdot \frac{1 - (n+1)\left(\frac{P}{P_s}\right)^n + n\left(\frac{P}{P_s}\right)^{n+1}}{1 + (b-1)\frac{P}{P_s} - b\left(\frac{P}{P_s}\right)^{n+1}} \tag{2}$$

where $q$ refers to the adsorbate adsorption capacity (mg $g^{-1}$), $Q_m$ is the maximum adsorption capacity (mg $g^{-1}$), $k_a$, $n_1$, $n$, and $b$ are the constants for the model, $P$ is the equilibrium pressure (kPa), and $P_s$ is the gas-phase pressure at saturation.

**Thermodynamics of Adsorption.** The isosteric heat of adsorption (*Qst*) is calculated by Clausius−Clapeyron equation, and is defined as eq 3,[48] which is calculated by measuring the gas adsorption isotherm at different temperatures.


https://doi.org/10.1021/acsomega.1c04618
ACS Omega 2021, 6, 30716−30725

$$Qst = RT^2\left(\frac{\partial \ln P}{\partial T}\right)_q \quad (3)$$

where $Qst$ refers to the isosteric heat of adsorption (kJ $mol^{-1}$), $R$ refers to the universal gas constant (kJ $mol^{-1}$ $K^{-1}$), $T$ is the adsorption temperature (K), $P$ is the adsorption pressure (kPa), and $q$ refers to the adsorption capacity (mmol $g^{-1}$).

## ■ ASSOCIATED CONTENT

### Supporting Information

The Supporting Information is available free of charge at https://pubs.acs.org/doi/10.1021/acsomega.1c04618.

TGA curves of urea, ACFs + urea and ACFs; the relation between acetone adsorption capacity and $S_{BET}$, pore volume ($V_{total}$, $V_{2-5\ nm}$, $V_{<2\ nm}$) and functional group content (oxygen, nitrogen); the fitting results of L−F model and *n*-layer BET model for acetone; the relation between $CO_2$ uptake and $S_{BET}$, pore volume ($V_{total}$, $V_{0.9\ nm}$) and functional group content (oxygen and nitrogen, nitrogen, oxygen); fitting parameters of the L−F model for $CO_2$ (PDF)

## ■ AUTHOR INFORMATION


### Corresponding Authors

**Zheng Zeng** − *School of Energy Science and Engineering, Central South University, Changsha 410083 Hunan, China*; Email: hdzengzheng@163.com

**Liqing Li** − *School of Energy Science and Engineering, Central South University, Changsha 410083 Hunan, China*; orcid.org/0000-0001-8297-309X; Email: liqingli@hotail.com

### Authors

**Rui Shi** − *School of Energy Science and Engineering, Central South University, Changsha 410083 Hunan, China; School of Civil Engineering, Inner Mongolia University of Technology, Hohhot 010051 Inner Mongolia, China*

**Baogen Liu** − *School of Energy Science and Engineering, Central South University, Changsha 410083 Hunan, China*

**Yuwei Jiang** − *School of Energy Science and Engineering, Central South University, Changsha 410083 Hunan, China*

**Xiang Xu** − *School of Energy Science and Engineering, Central South University, Changsha 410083 Hunan, China*

**Huijun Wang** − *School of Energy Science and Engineering, Central South University, Changsha 410083 Hunan, China*

Complete contact information is available at: https://pubs.acs.org/10.1021/acsomega.1c04618


### Author Contributions

R.S., L.L., and Z.Z. designed the study. R.S., B.L., and Y.J. conducted sample collection and data analysis. R.S. drafted the manuscript. B.L., X.X., H.W., and L.L. provided the suggestions for this study. R.S., L.L., and Z.Z. revised the manuscript.

### Notes

The authors declare no competing financial interest.

## ■ ACKNOWLEDGMENTS

This work was supported by the National Natural Science Foundation of China (No. 21878338); the National Key Technologies Research and Development Program of China (2019YFC0214302); the Key Research and Development Project of Hunan Province, China (2018SK2038); and the Natural Science Foundation of Inner Mongolia University of Technology (ZY202006).

## ■ REFERENCES


(1) Ma, X.; Chen, R.; Zhou, K.; Wu, Q.; Li, H.; Zeng, Z.; Li, L. Activated Porous Carbon with an Ultrahigh Surface Area Derived from Waste Biomass for Acetone Adsorption, $CO_2$ Capture, and Light Hydrocarbon Separation. *ACS Sustainable Chem. Eng.* **2020**, *8*, 11721−11728.

(2) Yang, P.; Rao, L.; Zhu, W.; Wang, L.; Ma, R.; Chen, F.; Lin, G.; Hu, X. Porous Carbons Derived from Sustainable Biomass via a Facile One-Step Synthesis Strategy as Efficient $CO_2$ Adsorbents. *Ind. Eng. Chem. Res.* **2020**, *59*, 6194−6201.

(3) Li, Q.; Liu, S.; Wang, L.; Chen, F.; Shao, J.; Hu, X. Efficient nitrogen doped porous carbonaceous $CO_2$ adsorbents based on lotus leaf. *J. Environ. Sci.* **2021**, *103*, 268−278.

(4) Wang, D. F.; Wang, Z. Q.; Zheng, X. H.; Tian, M. W. Activated carbon fiber derived from the seed hair fibers of Metaplexis japonica: Novel efficient adsorbent for methylene blue. *Ind. Crops Prod.* **2020**, *148*, No. 112319.

(5) Hassan, M. F.; Sabri, M. A.; Fazal, H.; Hafeez, A.; Shezad, N.; Hussain, M. Recent trends in activated carbon fibers production from various precursors and applications-A comparative review. *J. Anal. Appl. Pyrolysis* **2020**, *145*, No. 104715.

(6) Chiang, Y. C.; Juang, R. S. Surface modifications of carbonaceous materials for carbon dioxide adsorption: A review. *J. Taiwan Inst. Chem. Eng.* **2017**, *71*, 214−234.

(7) Li, X. Q.; Zhang, L.; Yang, Z. Q.; Wang, P.; Yan, Y. F.; Ran, J. Y. Adsorption materials for volatile organic compounds (VOCs) and the key factors for VOCs adsorption process: A review. *Sep. Purif. Technol.* **2020**, *235*, No. 116213.

(8) Liu, B. G.; Shi, R.; Ma, X. C.; Chen, R. F.; Zhou, K.; Xu, X.; Sheng, P.; Zeng, Z.; Li, L. Q. High yield nitrogen-doped carbon monolith with rich ultramicropores prepared by in-situ activation for high performance of selective $CO_2$ capture. *Carbon* **2021**, *181*, 270−279.

(9) Pang, R.; Lu, T.; Shao, J.; Wang, L.; Wu, X.; Qian, X.; Hu, X. Highly Efficient Nitrogen-Doped Porous Carbonaceous $CO_2$ Adsorbents Derived from Biomass. *Energy Fuels* **2021**, *35*, 1620−1628.

(10) Liu, S.; Rao, L.; Yang, P.; Wang, X.; Wang, L.; Ma, R.; Yue, L.; Hu, X. Superior $CO_2$ uptake on nitrogen doped carbonaceous adsorbents from commercial phenolic resin. *J. Environ. Sci.* **2020**, *93*, 109−116.

(11) Xu, X.; Guo, Y.; Shi, R.; Chen, H. Y.; Du, Y. K.; Liu, B. G.; Zeng, Z.; Yin, Z. Y.; Li, L. Q. Natural Honeycomb-like structure cork carbon with hierarchical Micro-Mesopores and N-containing functional groups for VOCs adsorption. *Appl. Surf. Sci.* **2021**, *565*, No. 150550.

(12) Hassani, A.; Khataee, A. R. Activated carbon fiber for environmental protection. In *Activated Carbon Fiber and Textiles*, Chen, J. Y., Ed.; Woodhead Publishing Series in Textiles, 2017; pp 245−280.

(13) Bai, Y.; Huang, Z. H.; Kong, F. Y. Electrospun preparation of microporous carbon ultrafine fibers with tuned diameter, pore structure and hydrophobicity from phenolic resin. *Carbon* **2014**, *66*, 705−712.

(14) Oh, G. Y.; Ju, Y. W.; Kim, M. Y.; Jung, H. R.; Kim, H. J.; Lee, W. J. Adsorption of toluene on carbon nanofibers prepared by electrospinning. *Sci. Total Environ.* **2008**, *393*, 341−347.

(15) Ma, X. C.; Li, L. Q.; Chen, R. F.; Wang, C. H.; Zhou, K.; Li, H. L. Porous carbon materials based on biomass for acetone adsorption: Effect of surface chemistry and porous structure. *Appl. Surf. Sci.* **2018**, *459*, 657−664.

(16) Nan, D.; Liu, J.; Ma, W. Electrospun phenolic resin-based carbon ultrafine fibers with abundant ultra-small micropores for $CO_2$ adsorption. *Chem. Eng. J.* **2015**, *276*, 44−50.

(17) Teo, W. E.; Inai, R.; Ramakrishna, S. Technological advances in electrospinning of nanofibers. *Sci. Technol. Adv. Mater.* **2011**, *12*, No. 013002.

(18) Dincer, K.; Waisi, B.; Onal, G.; Tugluoglu, N.; McCutcheon, J.; Yuksel, O. F. Investigation of optical and dispersion parameters of electrospinning grown activated carbon nanofiber (ACNF) layer. *Synth. Met.* **2018**, *237*, 16−22.

(19) Zhang, H. N.; Xie, Y. X.; Song, Y.; Qin, X. H. Preparation of high-temperature resistant poly (m-phenylene isophthalamide)/polyacrylonitrile composite nanofibers membrane for air filtration. *Colloids Surf., A* **2021**, *624*, No. 126831.
(20) Qi, Y.; Zhang, X. X.; Yang, J. X.; Shi, K.; Li, J.; Zhang, S. Effects of the molecular structure from pitch fractions on the properties of pitch-based electrospun nanofibers. *J. Appl. Polym. Sci.* **2021**, *138*, No. 50728.
(21) Khan, K. U.; Mahmood, S.; Raees, A.; Rizvi, G. A postgraduate experiment: a study of fabricating nanofibers by electrospinning. *Eur. J. Phys.* **2021**, *42*, No. 045501.
(22) Wang, X.-F.; Xiong, L.; Zhong, J.-J.; Jin, L.; Yan, J.-L.; Mu, B.; Zhang, Y.-G.; Song, S.-L. Nitrogen-Containing Porous Carbon Fibers Prepared from Polyimide Fibers for $CO_2$ Capture. *Ind. Eng. Chem. Res.* **2020**, *59*, 18106−18114.
(23) Gao, J.; Li, L. Q.; Zeng, Z.; Ma, X. C.; Chen, R. F.; Wang, C. H.; Zhou, K. Superior acetone uptake of hierarchically N-doped potassium citrate-based porous carbon prepared by one-step carbonization. *J. Mater. Sci.* **2019**, *54*, 6186−6198.
(24) Chen, R. F.; Han, N.; Li, L. Q.; Wang, S. B.; Ma, X. C.; Wang, C. H.; Li, H. L.; Li, H. Y.; Zeng, L. Fundamental understanding of oxygen content in activated carbon on acetone adsorption desorption. *Appl. Surf. Sci.* **2020**, *508*, No. 145211.
(25) Meng, F. Y.; Song, M.; Wei, Y. X.; Wang, Y. L. The contribution of oxygen-containing functional groups to the gas-phase adsorption of volatile organic compounds with different polarities onto lignin-derived activated carbon fibers. *Environ. Sci. Pollut. Res.* **2019**, *26*, 7195−7204.
(26) Tsubouchi, N.; Nishio, M.; Mochizuki, Y. Role of nitrogen in pore development in activated carbon prepared by potassium carbonate activation of lignin. *Appl. Surf. Sci.* **2016**, *371*, 301−306.
(27) Lee, D. W.; Jin, M. H.; Oh, D.; Lee, S. W.; Park, J. S. Straightforward Synthesis of Hierarchically Porous Nitrogen-Doped Carbon via Pyrolysis of Chitosan/Urea/KOH Mixtures and Its Application as a Support for Formic Acid Dehydrogenation Catalysts. *ACS Sustainable Chem. Eng.* **2017**, *5*, 9935−9944.
(28) Li, D. W.; Ma, T. F.; Zhang, R. L.; Tian, Y. Y.; Qiao, Y. Y. Preparation of porous carbons with high low-pressure $CO_2$ uptake by KOH activation of rice husk char. *Fuel* **2015**, *139*, 68−70.
(29) Jia, M. Y.; Geng, S. T.; Jiang, Q. T.; Xu, C. R.; Zhang, Y.; Yin, G. C.; Jia, F. C.; Wang, X. M.; Zhou, T.; Liu, B. A strategy to prepare activated carbon fiber membranes for flexible solid-state supercapacitor applications. *J. Mater. Sci.* **2021**, *56*, 3911−3924.
(30) Suhdi; Wang, S. C. Fine Activated Carbon from Rubber Fruit Shell Prepared by Using $ZnCl_2$ and KOH Activation. *Appl. Sci.* **2021**, *11*, No. 3994.
(31) Zhang, X. T.; Chen, W. X. Mechanisms of pore formation on multi-wall carbon nanotubes by KOH activation. *Microporous Mesoporous Mater.* **2015**, *206*, 194−201.
(32) Yoshikawa, Y.; Teshima, K.; Futamura, R.; Tanaka, H.; Neimark, A. V.; Kaneko, K. Structural mechanism of reactivation with steam of pitch-based activated carbon fibers. *J. Colloid Interface Sci.* **2020**, *578*, 422−430.
(33) Meng, L. Y.; Park, S. J. Effect of heat treatment on $CO_2$ adsorption of KOH-activated graphite nanofibers. *J. Colloid Interface Sci.* **2010**, *352*, 498−503.
(34) Lueking, A. D.; Pan, L.; Narayanan, D. L.; Clifford, C. E. B. Effect of expanded graphite lattice in exfoliated graphite nanoribers on hydrogen storage. *J. Phys. Chem. B* **2005**, *109*, 12710−12717.
(35) Yu, J. Y.; Guo, M. Y.; Muhammad, F.; Wang, A. F.; Zhang, F.; Li, Q.; Zhu, G. S. One-pot synthesis of highly ordered nitrogen-containing mesoporous carbon with resorcinol-urea-formaldehyde resin for $CO_2$ capture. *Carbon* **2014**, *69*, 502−514.
(36) Ju, C.P.; Don, J.; Tlomak, P. Transmission electron microscopic study of three-dimensional polyacrylonitrile fibre-mesophase pitch matrix carbon-carbon composite. *J. Mater. Sci.* **1991**, *26*, 6753−6758.
(37) Qian, X.; Wang, X. F.; Zhong, J. J.; Zhi, J. H.; Heng, F. F.; Zhang, Y. G.; Song, S. L. Effect of fiber microstructure studied by Raman spectroscopy upon the mechanical properties of carbon fibers. *J. Raman Spectrosc.* **2019**, *50*, 665−673.
(38) Kukobat, R.; Minami, D.; Hayashi, T.; Hattori, Y.; Matsuda, T.; Sunaga, M.; Bharti, B.; Asakura, K.; Kaneko, K. Sol-gel chemistry mediated Zn/Al-based complex dispersant for SWCNT in water without foam formation. *Carbon* **2015**, *94*, 518−523.
(39) Chen, H. Y.; Guo, Y.; Du, Y. K.; Xu, X.; Su, C. Q.; Zeng, Z.; Li, L. Q. The synergistic effects of surface functional groups and pore sizes on $CO_2$ adsorption by GCMC and DFT simulations. *Chem. Eng. J.* **2021**, *415*, No. 128824.
(40) Ma, X. C.; Li, L. Q.; Zeng, Z.; Chen, R. F.; Wang, C. H.; Zhou, K.; Su, C. Q.; Li, H. L. Synthesis of nitrogen-rich nanoporous carbon materials with $C_3N$-type from ZIF-8 for methanol adsorption. *Chem. Eng. J.* **2019**, *363*, 49−56.
(41) Everett, D. H.; Powl, J. C. Adsorption in slit-like and cylindrical micropores in the henry's law region. A model for the microporosity of carbons. *J. Chem. Soc., Faraday Trans. 1.* **1976**, *0*, 3901−4366.
(42) Li, D. H.; Li, L. Q.; Chen, R. F.; Wang, C. H.; Li, H. L.; Li, H. Y. A MIL-101 Composite Doped with Porous Carbon from Tobacco Stem for Enhanced Acetone Uptake at Normal Temperature. *Ind. Eng. Chem. Res.* **2018**, *57*, 6226−6235.
(43) Li, L. Q.; Ma, X. C.; Chen, R. F.; Wang, C. H.; Lu, M. M. Nitrogen-Containing Functional Groups-Facilitated Acetone Adsorption by ZIF-8-Derived Porous Carbon. *Materials* **2018**, *11*, No. 159.
(44) Liu, Z.; Luo, J. Y.; Peng, Y.; Yang, Y. H.; Zeng, Z.; Li, L. Q. Preparation of Phosphorus-containing Porous Carbon by Direct Carbonization for Acetone Adsorption. *Colloids Surf., A* **2020**, *606*, No. 125431.
(45) Sevilla, M.; Falco, C.; Titirici, M. M.; Fuertes, A. B. High-performance $CO_2$ sorbents from algae. *RSC Adv.* **2012**, *2*, 12792−12797.
(46) Dil, E. A.; Ghaedi, M.; Asfaram, A.; Hajati, S.; Mehrabi, F.; Goudarzi, A. Preparation of nanomaterials for the ultrasound-enhanced removal of Pb2+ ions and malachite green dye: Chemometric optimization and modeling. *Ultrason. Sonochem.* **2017**, *34*, 677−691.
(47) Benadjemia, M.; Milliere, L.; Reinert, L.; Benderdouche, N.; Duclaux, L. Preparation, characterization and Methylene Blue adsorption of phosphoric acid activated carbons from globe artichoke leaves. *Fuel Process. Technol.* **2011**, *92*, 1203−1212.
(48) Wang, J. C.; Senkovska, I.; Oschatz, M.; Lohe, M. R.; Borchardt, L.; Heerwig, A.; Liu, Q.; Kaskel, S. Highly porous nitrogen-doped polyimine-based carbons with adjustable microstructures for $CO_2$ capture. *J. Mater. Chem. A* **2013**, *1*, 10951−10961.
(49) Khalili, S.; Khoshandam, B.; Jahanshahi, M. Synthesis of activated carbon/polyaniline nanocomposites for enhanced $CO_2$ adsorption. *RSC Adv.* **2016**, *6*, 35692−35704.
(50) Kirbiyikkurukavak, Ç.; Buyukbekar, B. Z.; Ersoz, M. PAN-based activated carbon nanofiber/metal oxide composites for $CO_2$ and $CH_4$ adsorption: influence of metal oxide. *Turk J Chem* **2021**, *45*, 914−926.
(51) Othman, F. E. C.; Yusof, N.; Samitsu, S.; Abdullah, N.; Hamid, M. F.; Nagai, K.; Abidin, M. N. Z.; Azali, M. A.; Ismail, A. F.; Jaafar, J.; Aziz, F.; Salleh, W. N. W. Activated carbon nanofibers incorporated metal oxides for $CO_2$ adsorption: Effects of different type of metal oxides. *J. CO2 Util.* **2021**, *45*, No. 101434.
(52) Wang, L.; Li, J.; Gan, G.; Fan, S.; Chen, X.; Liang, F.; Wei, L.; Zhang, Z.; Hao, Z.; Li, X. Activated Carbon Fibers Prepared by One-Step Activation with $CuCl_2$ for Highly Efficient Gas Adsorption. *Ind. Eng. Chem. Res.* **2020**, *59*, 19793−19802.
(53) An, L.; Liu, S.; Wang, L.; Wu, J.; Wu, Z.; Ma, C.; Yu, Q.; Hu, X. Novel Nitrogen-Doped Porous Carbons Derived from Graphene for Effective $CO_2$ Capture. *Ind. Eng. Chem. Res.* **2019**, *58*, 3349−3358.
(54) Matthews, M. J.; Pimenta, M. A.; Dresselhaus, G.; Dresselhaus, M. S.; Endo, M. Origin of dispersive effects of the Raman D band in carbon materials. *Phys. Rev. B* **1999**, *59*, R6585−R6588.
(55) Sun, X. J.; Xia, Q. B.; Zhao, Z. X.; Li, Y. W.; Li, Z. Synthesis and adsorption performance of MIL-101(Cr)/graphite oxide composites with high capacities of n-hexane. *Chem. Eng. J.* **2014**, *239*, 226−232.
(56) Saadi, R.; Saadi, Z.; Fazaeli, R.; Fard, N. E. Monolayer and multilayer adsorption isotherm models for sorption from aqueous media. *Korean J. Chem. Eng.* **2015**, *32*, 787−799.


https://doi.org/10.1021/acsomega.1c04618
*ACS Omega* 2021, 6, 30716−30725